

Dominant scattering mechanisms in the low/high electric field transport in cryogenic 2D confinement in Silicon (110) with high- κ oxides

Hsin-Wen Huang¹, Xi-Jun Fang¹, Edward Chen² and Yuh-Renn Wu^{1*}

¹Graduate Institute of Photonics and Optoelectronics and Department of Electrical Engineering, National Taiwan University, Sec.4, Roosevelt Rd., Taipei 10617, Taiwan.

²Corporate Research, Taiwan Semiconductor Manufacturing Company Ltd., 168, Kehuan Rd., Baoshan Township, Hsinchu County 308-001, Taiwan.

E-mail: yrwu@ntu.edu.tw

March 2026

Abstract. The performance of silicon nano-devices at cryogenic temperatures is critical for quantum qubit control circuits and space applications. Using multi-valley Monte Carlo simulations, we investigate electron transport in Si (110) systems. At low electric fields, phonon absorption becomes negligible, and mobility is governed by competition between remote Coulomb scattering (RCS) at low inversion charge density and surface roughness scattering (SRS) at high density, leading to a mobility peak. High- κ dielectrics such as HfO₂ introduce remote phonon scattering (RPS), which suppresses mobility. Under high electric fields, phonon emission dominates at 4 K, limiting velocity enhancement and resulting in limited current improvement.

Keywords: Cryogenic system, Mobility, Silicon (110) confinement, Monte Carlo method

1. Introduction

Cryogenic metal oxide semiconductor field-effect transistors (MOSFETs) are essential for peripheries of a quantum computer and are also relevant to deep-space and satellite electronic applications [1, 2, 3, 4]. Understanding two-dimensional (2D) electron transport under silicon (110) confinement is crucial for advancing cryogenic FinFET and other nonplanar silicon technologies, where carrier transport strongly depends on surface orientation and body thickness [5, 6]. Previous studies have investigated the temperature dependence of electron mobility in bulk MOSFETs under (100) and (110) field-induced quantum confinement with SiO₂ and HfO₂ gate dielectrics [7, 8, 9]. Furthermore, cryogenic operation of FinFET devices has been explored in several experimental and modeling studies [10, 11, 12]. However, detailed investigations of electron transport under Si(110) confinement in advanced FinFET geometries remain limited. Moreover, the field-dependent velocity is important due to the short channel lengths in the tens of nanometers [13]. This work employs multi-subband Monte Carlo simulation to investigate electron mobility in silicon (110) confinement under cryogenic conditions. By incorporating quantum confinement effects and solving the Poisson-Schrödinger equations, the dominant scattering rates and their impact on transport properties have been analyzed. Our results reveal that surface roughness and Coulomb scattering dominate at low temperatures, while high- κ dielectrics introduce additional mobility-limiting factors. These findings provide valuable insights for cryogenic semiconductor design and nanoelectronic applications.

2. Methodology

This study focuses on electron mobility in silicon (110) confinement systems under cryogenic conditions. Figure 1 shows the FinFET structure [14] studied in this paper. As shown in Fig. 1, the lateral confinement at each position is calculated, and the corresponding wave functions are used for the scattering-rate evaluation. To model carrier transport, we employed a multi-valley Monte Carlo method. To begin with, considering the quantum confinement effect, we calculate the effective mass and sub-bands [15]. Then, the Poisson and Schrödinger equations were solved to acquire the wave function as shown in Fig.1. In particular, we apply the localized

landscape model [16] to obtain the effective quantum potential, which is easier to couple with the Poisson and drift-diffusion solver, and we can obtain a better-converged result. Further, these wave functions were then utilized to calculate scattering rates for various mechanisms, including (1) acoustic phonon scattering (APS) [17], (2) optical phonon scattering (OPS), (3) remote phonon scattering (RPS) [18, 19, 20], (4) surface roughness scattering (SRS) [21, 22, 23], (5) remote Coulomb scattering (RCS) [24, 25], and (6) ionized impurity scattering (IIS)[26]. To compute the scattering rates, we applied Fermi's Golden Rule [27, 28], which is given by:

$$W(k, k') = \frac{2\pi}{\hbar} |M_{kk'}|^2 \delta(E_{k'} - E_k) \quad (1)$$

In this equation, $W(k, k')$ represents the scattering rate for a transition from the initial state k to the final state k' , $M_{kk'}$ denotes the matrix element of the scattering process, and $\delta(E_{k'} - E_k)$ means the energy conservation.

The Monte Carlo [29, 30] simulation tracks individual carriers through random sampling of scattering events, accounting for interactions with phonons, ionized impurities, and the surrounding material. This approach provides a detailed view of carrier dynamics, capturing the effects of complex interactions, particularly at low temperatures where phonon-related scattering diminishes and other mechanisms, like surface roughness and Coulomb scattering, become dominant.

The simulation results are validated by comparing the calculated electron mobility under various temperature and carrier concentration conditions. The numerical parameters associated with each scattering mechanism are specified at their first occurrence. All Monte Carlo simulation settings used in this study are summarized in the Supplementary Information (Table. S1). The numerical parameters used in this work are not unique fitting values but are employed as model parameters to define a consistent baseline for identifying dominant scattering mechanisms. The qualitative transport trends are mainly governed by the relative balance among the different scattering mechanisms.

3. Results and Discussion

Fig. 2 shows the scattering rates of every scattering mechanism in our model with different temperatures. As shown in Fig. 2, phonon-caused scattering is crucial

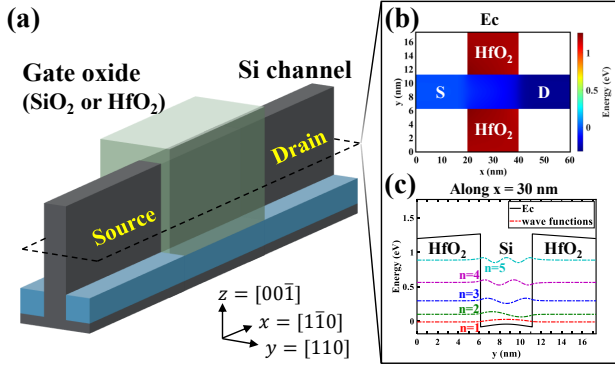


Figure 1. (a) The FinFET structure used in this study. The quantum confinement is in the (110) direction. (b) shows the E_c of the channel at the cross section. (c) shows the conduction band profile and the calculated subband energies, together with their corresponding wave functions, obtained from the Poisson and Schrödinger solver along the cross section shown in (b).

when discussing the electron transport property. Since the phonon is oriented from the thermal fluctuation, the electron-phonon scattering rate is highly related to the environment temperature. Fig. 2(a) is the acoustic phonon scattering rates of the silicon (110) confinement system. The detailed parameters used in the calculation are from Refs. [24, 31]. The device in Ref. [31] is like a tri-gates structure, and the deformation potential the researcher used is 6.27 eV. However, in terms of SOI, Esseni found the value should be 14.6 eV [24], and this condition is more similar to our study. Therefore, 14.6 eV is chosen as the deformation potential in our calculation. As a result, the scattering rate decreases as the temperature decreases. Fig. 2(b) is the optical phonon scattering rates, including the intravalley and equivalent inter-valleys transitions (f and g scattering) by emitting or absorbing an optical phonon energy. As the temperature decreases, the electron optical phonon emission scattering dominates. As the temperature is below 50K, the electron-phonon emission scattering is directly related to carrier energy instead of phonon occupations. The phonon absorption scattering is diminished at low K.

For better gate control in the channel, high- κ materials such as HfO_2 are applied as the dielectric layer. However, these materials can introduce remote phonon scattering, which has been reported to degrade carrier mobility [19]. In this study, we discuss the remote phonon scattering effect by comparing the conditions of two different oxide materials (SiO_2 and HfO_2) as the dielectric. Fig. 2(c) represents the remote phonon scattering rates. The parameters used in remote phonon scattering rate calculation are from Refs. [15, 16]. From the FinFET structure, we can simplify our simulation into the double gates condition.

That is, the top and bottom dielectrics sandwich the silicon channel. The material of both sides of the oxide is the same. The width of the channel is set as 5 nm, and the thickness of the oxide is 1 nm. Compared with oxides in our SiO_2 case, the HfO_2 one has a much higher scattering rate. This is because of the large dielectric constant at low frequency.

Surface roughness scattering occurs when electrons move around the interface of two materials. The imperfection surface causes fluctuations in the potential energy landscape, leading to scattering events that affect the motion of the electrons, and this mechanism is independent of the temperature. Fig. 2(d) is the scattering rate of the surface roughness.

Remote Coulomb scattering is induced from the charges located in the oxide or at the oxide-semiconductor interface. Due to the potential propagation of the remote Coulomb, the carrier's transport property in the channel is influenced. Since the Coulomb force is related to the distance between the oxide charges and channel carriers, knowing the distribution of the carriers in the channel is vital. Therefore, we chose a similar 2D electron gas density in the inversion layer (n_{inv}) under temperatures (around $1.0 \times 10^{12} \text{ cm}^{-2}$) and assumed the fix-charges density is $2.0 \times 10^{13} \text{ cm}^{-2}$. Fig. 2(e) shows the remote Coulomb scattering rate. The decrement of the scattering rate as the temperatures lowered resulted from the increment of the screening effect at low temperatures. The physics of ionized impurity scattering is similar to the remote Coulomb scattering. Ionized impurities form the scattering potential due to the Coulomb force. Compared with the remote Coulomb scattering, the charges causing the potential located in the channel. We also chose a similar n_{inv} layer concentration (around $1.0 \times 10^{12} \text{ cm}^{-2}$) and assumed that the impurity density is $5.0 \times 10^{11} \text{ cm}^{-2}$ in the 5 nm channel. Fig. 2(f) shows the ionized impurity scattering rate. The decrement of the scattering rate as the temperatures lowered is also due to the increment of the screening effect at low temperatures.

If the device is under a different bias, the n_{inv} changes in the channel. Thus, the surface roughness scattering rate, remote Coulomb scattering rate, and ionized impurity scattering rate are influenced. Figs. 3(a) and 3(b) are the results of surface roughness scattering rate, remote Coulomb scattering rate, and ionized impurity scattering rate with various n_{inv} . Regarding the surface roughness scattering rate, the scattering rate enhanced as the inversion concentration increased. That is, a higher n_{inv} usually means more electrons are induced by gate bias and attracted to the Oxide/Si interfaces, which are more easily affected by the surface roughness. The rate decreases as the

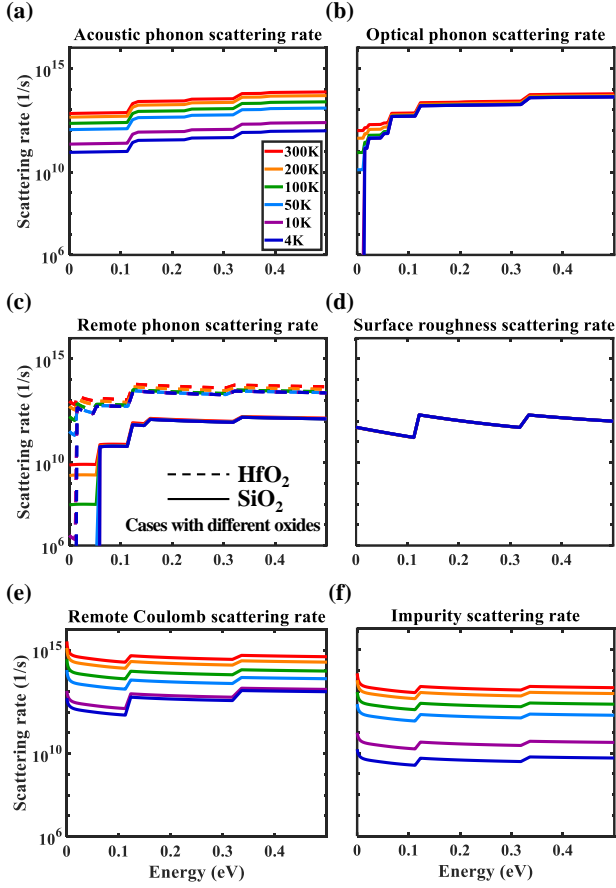


Figure 2. Scattering rates with electron energy. (a) Acoustic phonon. (b) Optical phonon. Intravalley and inter-valley transitions are included. (c) Remote phonon. The dashed lines are the result that HfO_2 is the dielectric, and the solid lines show that SiO_2 is used. (d) Surface roughness. The surface roughness parameters λ is 1.0 nm and Δ is 0.5 nm. (e) Remote Coulomb. The fix-charge density in the oxide is $2.0 \times 10^{13} \text{ cm}^{-2}$ and the charges position is 1 nm away from the interface. (f) Impurity. The ionized impurity concentration is set as $5.0 \times 10^{11} \text{ cm}^{-2}$.

inversion layer concentration rises for remote Coulomb scattering and ionized impurity scattering rates due to carrier screening. Higher n_{inv} represents the stronger screening effect. Therefore, fewer scattering events happen at a higher n_{inv} . Figs. 3(c) and 3(d) show the electron mobility with various n_{inv} under temperatures as the oxide is SiO_2 or HfO_2 (the same effective oxide thickness (EOT) is used). From the results, we can observe a peak mobility for n_{inv} near 10^{12} cm^{-2} to $5.0 \times 10^{12} \text{ cm}^{-2}$ at different temperatures. This phenomenon results from the competition between surface roughness scattering and remote Coulomb scattering. The remote Coulomb scattering rate dominates at small n_{inv} due to weaker screening. The surface roughness scattering rate increases the n_{inv} increase due to the higher electron distribution around the surface. This crossover behavior is further clarified

in the Supplementary Information (Fig. S2), where the individual mobility contributions are evaluated by selectively enabling different scattering mechanisms, explicitly showing the transition from Coulomb-limited transport at low n_{inv} to surface-roughness-limited transport at high n_{inv} .

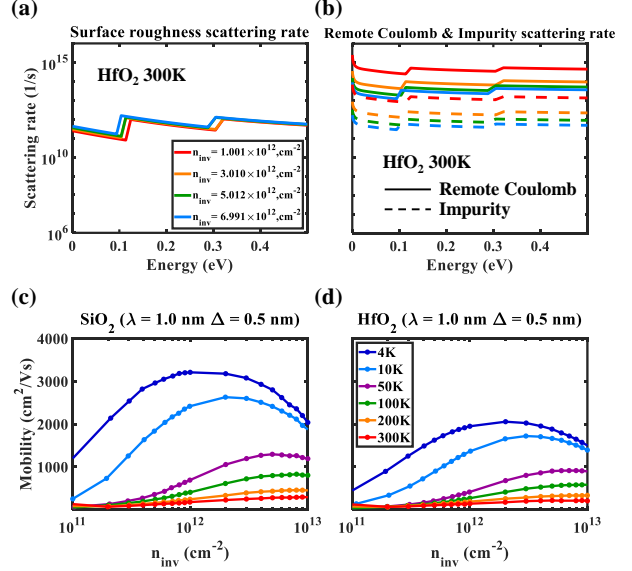


Figure 3. (a) Surface roughness scattering rate ($\lambda = 1.0 \text{ nm}$ and $\Delta = 0.5 \text{ nm}$) with different inversion layer concentrations (n_{inv}). (b) Remote Coulomb (solid lines, fix-charge concentration = $2.0 \times 10^{13} \text{ cm}^{-2}$) and ionized impurity scattering (dash lines, impurity concentration = $5.0 \times 10^{11} \text{ cm}^{-2}$) rates with n_{inv} . (c) Mobility with various n_{inv} and SiO_2 is the dielectric. (d) Mobility with various n_{inv} and HfO_2 is the dielectric. In (c) and (d), the same surface roughness parameters and fix-charge and impurity concentrations as (a) and (b) are set.

Figs. 4 (a) and 4(b) show the overall scattering rate changes with n_{inv} under 300K and 4K by using SiO_2 as oxide. To begin with, at 4K, the phonon-related scattering rate magnitudes (green curve) are lower than those at 300K. Moreover, a competition between remote Coulomb scattering and surface roughness scattering (red and blue curves, respectively) can be observed with different n_{inv} . At low n_{inv} , remote Coulomb scattering dominates. With the rise of n_{inv} , the surface roughness rate increases, and remote Coulomb scattering becomes lower. As the n_{inv} is larger, the surface roughness scattering rate approaches the magnitude of the remote Coulomb scattering rate. In terms of the ratio of these two mechanisms to the total scattering rate, since the phonon scattering rate is higher at 300K, the mobility changes owing to the alternation of these two mechanisms are not that obvious compared with the case under 4K. Furthermore, a higher remote phonon scattering rate (purple curve) is observed in the HfO_2

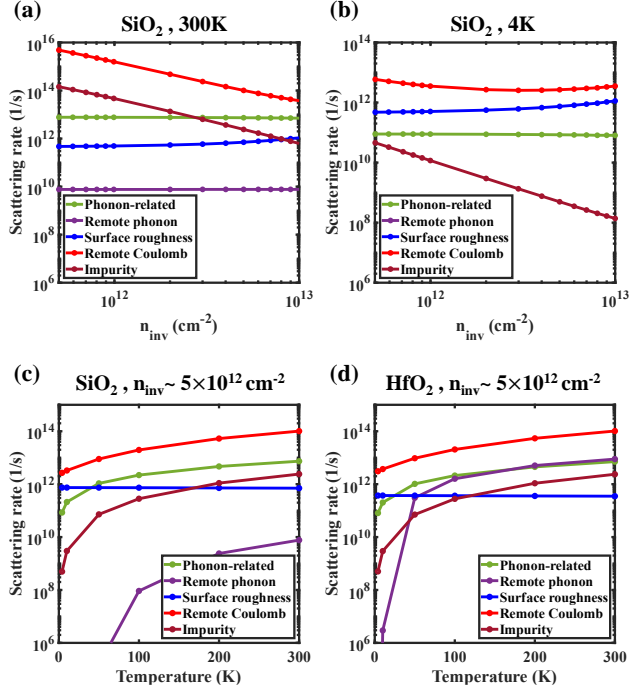


Figure 4. (a)~(b) Scattering rates (electron energy = 0.001 eV) with n_{inv} by using SiO_2 as dielectric at 300K and 4K, respectively. (c)~(d) Scattering rates (electron energy = 0.001 eV) with temperatures and SiO_2 and HfO_2 are used as dielectric, respectively. The same parameters in Fig. 2 are set.

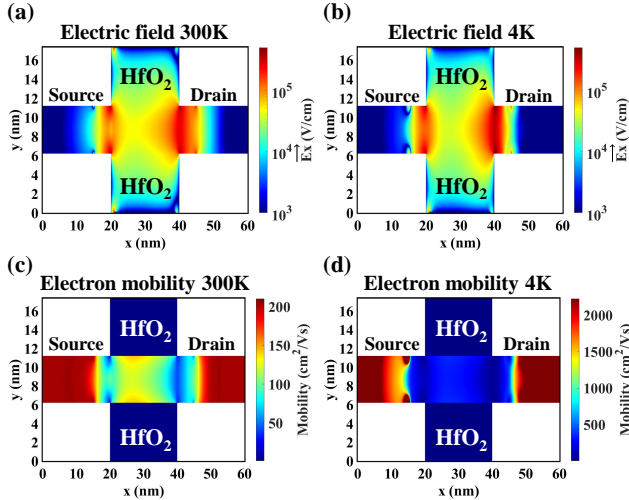


Figure 5. (a) and (b) show the Electric field in the transport direction, \vec{E}_x , in the channel at 300K and 4K, respectively. (c) and (d) show the resulted effective high field mobility along the channel at 300K and 4K, respectively.

case than in the SiO_2 case, as shown in Figs. 4(c) and 4(d). Then, we discuss the scattering rates change with temperatures under $n_{\text{inv}} \sim 5.0 \times 10^{12} \text{ cm}^{-2}$. We realize that as the temperature decreases, except for surface roughness scattering, the other mechanisms' scattering rates decline. For phonon-related scattering, this is

because of the less heat fluctuation. This phenomenon is due to the higher screening effect in low temperatures for remote Coulomb and ionized impurity scattering. The individual phonon-related scattering components are shown in the Supplementary Information (Fig. S3).

The aforementioned discussion is based on the electron performance under a low electric field, $\vec{E} \parallel$, along the transport direction. For transistor applications, especially in short gate-length cases, the electric field along the channel becomes very large, causing the electron velocity to reach saturation. Figures 5(a) and 5(b) show the electric field, $\vec{E}x$, along the channel. It can be observed that the electric field may exceed 10^5 V/cm in the short-channel case. The effective mobility along the channel is therefore not governed by the low-field mobility but is instead influenced by the high-field velocity at each location. As a result, the current density is mainly determined by these high-field velocities, making it important to further investigate this effect. Figs. 6(a) and 6(b) show the field-dependent velocity result by using SiO_2 and HfO_2 as oxide with $n_{\text{inv}} \sim 5.0 \times 10^{12} \text{ cm}^{-2}$, and the electron performance in the higher electric field can be investigated. These plots show that the field-dependent velocity reaches a peak around or larger than (depending on the temperature) the electric field is $1.0 \times 10^5 \text{ V/cm}$. In addition, there is another peak in the HfO_2 case at low temperatures (electric field $\sim 1.0 \times 10^4 \text{ V/cm}$). We record the scattering events to study which scattering mechanism causes this phenomenon. Figs. 6(c) and 6(d) are the event ratio of the main scattering mechanisms. From Figs. 6(c) and 6(d), we realize that the peak around or above $\sim 1.0 \times 10^5 \text{ V/cm}$ is resulted from the abrupt increment of g-type intervalley scattering (optical-phonon-related transition). The electron triggers this phenomenon and emits the phonon energy around 62 meV, leading to g-type intervalley scattering. At lower electric fields preceding the main peak, a saddle point in the HfO_2 case under the low temperature at an electric field $\sim 1.0 \times 10^4 \text{ V/cm}$ is due to the occurrence of intervalley scattering, in which the electron emits the phonon energy around 19 meV (g-type and f-type intervalley scattering). To corroborate this interpretation, the carrier population fractions and average carrier kinetic energies at representative electric fields are examined in the Supplementary Information (Fig. S4). The extracted low-field and high-field transport parameters at 4 K are summarized in Table 1.

4. Conclusion

This study investigated electron transport properties in silicon (110) confinement systems under cryogenic

Table 1. Summary of characteristic low-field and high-field transport parameters extracted at 4 K for Si (110) confinement. Low-field mobility is evaluated at $E = 1.0 \times 10^3$ V/cm as a function of n_{inv} , while high-field parameters are extracted at $n_{\text{inv}} \approx 5.0 \times 10^{12}$ cm $^{-2}$.

Low-field transport		
Parameter	SiO ₂	HfO ₂
$n_{\text{inv}}^{\text{peak}}$ (cm $^{-2}$)	1×10^{12}	2×10^{12}
μ_{peak} (cm 2 /V·s)	3211.6	2257.3
High-field transport		
Parameter	SiO ₂	HfO ₂
E_{crit} (V/cm)	1.5×10^5	1.5×10^5
v_{sat} (cm/s)	1.91×10^7	1.85×10^7

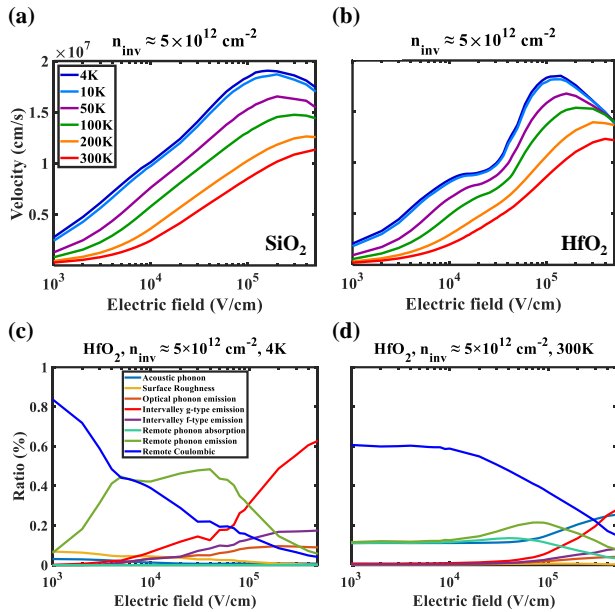


Figure 6. (a) and (b) represent the field-dependent velocity results that SiO₂ and HfO₂ are used as dielectric and the $n_{\text{inv}} \sim 5.0 \times 10^{12}$ cm $^{-2}$. (c) and (d) are the scattering events ratios of the main mechanisms when HfO₂ is the dielectric at 4K and 300K. The same parameters in Fig. 2 are set.

conditions using a multi-valley Monte Carlo simulation approach. The simulation framework accounted for various scattering mechanisms, including acoustic phonon, optical phonon, surface roughness, remote Coulomb, and ionized impurity scattering. Our results revealed the temperature dependence of these scattering rates, emphasizing the dominant role of surface roughness and Coulomb scattering at low temperatures where phonon-related scattering diminishes.

We also explored the impact of different dielectric materials (SiO₂ and HfO₂) on electron mobility. Our findings demonstrated that while high- κ materials like HfO₂ can enhance gate control and device performance, they also increase remote phonon

scattering rates compared to SiO₂. This trade-off suggests the need for optimized dielectric selection when designing cryogenic silicon devices.

Further analysis indicated that electron mobility behavior is influenced significantly by the inversion layer concentration (n_{inv}), with a clear competition between surface roughness and remote Coulomb scattering mechanisms. The results highlight that at lower inversion concentrations, remote Coulomb scattering dominates, but as n_{inv} increases, surface roughness scattering becomes more significant, reducing mobility. These insights provide a deeper understanding of the balance between scattering mechanisms in cryogenic environments.

Finally, the velocity versus electric field in the transport direction is studied. It revealed that optical phonon emission plays a crucial role in intervalley scattering, influencing the electron velocity profiles, especially under higher electric fields. These results validate the importance of considering both material and operational conditions when designing advanced silicon-based devices for low-temperature applications.

The data that supports the findings of this study are available from the corresponding author upon reasonable request.

Acknowledgments

This work is supported by the National Science and Technology Council under grant No. 112-2221-E-002-214-MY3, 113-2124-M-002-013-MY3, 114-2622-8-002 -016, and 113-2218-E-002-034. Dr. Yuh-Renn Wu is also supported by The Leap fellowship of the Foundation for the Advancement of Outstanding Scholarship.

References

- [1] Chiang H L, Hadi R A, Wang J F, Han H C, Wu J J, Hsieh H H, Horng J J, Chou W S, Lien B S and Chang C H 2023 How fault-tolerant quantum computing benefits from cryo-cmos technology *Proc. IEEE Symp. VLSI Technol. Circuits* pp 1–2
- [2] Hornibrook J, Colless J, Conway Lamb I, Pauka S, Lu H, Gossard A, Watson J, Gardner G, Fallahi S, Manfra M *et al.* 2015 *Physical Review Applied* **3** 024010
- [3] Hong S H, Choi G B, Baek R H, Kang H S, Jung S W and Jeong Y H 2008 *Low-temperature performance of nanoscale MOSFET for deep-space RF applications* Ph.D. thesis University of Warwick
- [4] Charbon E, Sebastiano F, Vladimirescu A, Homulle H, Visser S, Song L and Incandela R M 2016 Cryo-cmos for quantum computing *2016 IEEE international electron devices meeting (IEDM)* (IEEE) pp 13.5.1–13.5.4
- [5] Donetti L, Gámiz F, Rodríguez N, Jiménez-Molinos F and Roldán J 2010 *Solid-state electronics* **54** 191–195
- [6] Takagi S i, Toriumi A, Iwase M and Tango H 2002 *IEEE Transactions on Electron Devices* **41** 2363–2368
- [7] Masaki K, Taniguchi K, Hamaguchi C and Iwase M 1991 *Jpn. J. Appl. Phys.* **30** 2734

- [8] Zhu W and Ma T 2004 *IEEE Electron Device Letters* **25** 89–91 ISSN 0741-3106
- [9] Mereu B, Rossel C, Gusev E and Yang M 2006 *Journal of applied physics* **100** 014504 ISSN 0021-8979
- [10] Beckers A, Jazaeri F and Enz C 2018 *IEEE Transactions on Electron Devices* **65** 3617–3625
- [11] Homulle H, Song L, Charbon E and Sebastiano F 2018 *IEEE Journal of the Electron Devices Society* **6** 263–270
- [12] Pavanello M, Martino J, Simoen E and Claeys C 2009 *Cryogenics* **49** 590–594
- [13] Modelli A and Manzini S 1988 *Solid-state electronics* **31** 99–104
- [14] Hisamoto D, Lee W C, Kedzierski J, Takeuchi H, Asano K, Kuo C, Anderson E, King T J, Bokor J and Hu C 2000 *IEEE transactions on electron devices* **47** 2320–2325
- [15] Serra N and Esseni D 2010 *IEEE transactions on electron devices* **57** 482–490 ISSN 0018-9383
- [16] Li C K, Piccardo M, Lu L S, Mayboroda S, Martinelli L, Peretti J, Speck J S, Weisbuch C, Filoche M and Wu Y R 2017 *Physical Review B* **95** 144206 ISSN 2469-9950
- [17] Singh J 2007 *Electronic and optoelectronic properties of semiconductor structures* (Cambridge University Press) ISBN 1139440578
- [18] Ma Y X, Su H, Tang W M and Lai P T 2023 *Journal of Vacuum Science and Technology B* **41** 060804 ISSN 2166-2746
- [19] Fischetti M V, Neumayer D A and Cartier E A 2001 *Journal of Applied Physics* **90** 4587–4608 ISSN 0021-8979
- [20] Hu B 2015 *Physica B: Condensed Matter* **461** 118–121 ISSN 0921-4526
- [21] Ramayya E B, Vasileska D, Goodnick S and Knezevic I 2008 *Journal of Applied Physics* **104** 063711 ISSN 0021-8979
- [22] Ando T, Fowler A B and Stern F 1982 *Reviews of Modern Physics* **54** 437
- [23] Lombardi C, Manzini S, Saporito A and Vanzi M 1988 *IEEE Transactions on Computer-Aided Design of Integrated Circuits and Systems* **7** 1164–1171
- [24] Esseni D and Abramo A 2003 *IEEE Transactions on Electron Devices* **50** 1665–1674 ISSN 0018-9383
- [25] Gámiz F, López-Villanueva J, Jiménez-Tejada J, Melchor I and Palma A 1994 *Journal of applied physics* **75** 924–934 ISSN 0021-8979
- [26] Jung H, Ohtsuka H, Taniguchi K and Hamaguchi C 1996 *Journal of applied physics* **79** 2559–2565
- [27] Hugenholtz N 1957 *Physica* **23** 481–532 ISSN 0031-8914
- [28] Chuang S L 2012 *Physics of photonic devices* (John Wiley and Sons) ISBN 1118585658
- [29] Jacoboni C and Reggiani L 1983 *Reviews of modern Physics* **55** 645
- [30] Jacoboni C, Canali C, Ottaviani G and Quaranta A A 1977 *Solid-State Electronics* **20** 77–89
- [31] Thomas S M 2011 *Electrical characterisation of novel silicon MOSFETs and fnFETs* Ph.D. thesis University of Warwick